nature nanotechnology

SUPPLEMENTARY INFORMATION

https://doi.org/10.1038/s41565-018-0279-8

In the format provided by the authors and unedited.

Two-photon interference in the telecom C-band after frequency conversion of photons from remote quantum emitters

Jonas H. Weber[1,3], Benjamin Kambs[2,3], Jan Kettler[1], Simon Kern[1], Julian Maisch[1], Hüseyin Vural[1], Michael Jetter[1], Simone L. Portalupi[1*], Christoph Becher[2] and Peter Michler[1*]

[1]Institut für Halbleiteroptik und Funktionelle Grenzflächen, Center for Integrated Quantum Science and Technology (IQST) and SCoPE, University of Stuttgart, Stuttgart, Germany. [2]Fachrichtung Physik, Universität des Saarlandes, Saarbrücken, Germany. [3]These authors contributed equally: Jonas H. Weber, Benjamin Kambs. *e-mail: s.portalupi@ihfg.uni-stuttgart.de; p.michler@ihfg.uni-stuttgart.de

Supplementary information to "Two-photon interference in the telecom C-band after frequency conversion of photons from remote quantum emitters"

Jonas H. Weber,* Benjamin Kambs,* Jan Kettler, Simon Kern, Julian Maisch, Hüseyin Vural, Michael Jetter, Simone L. Portalupi,† Christoph Becher, and Peter Michler‡

(Dated: 2018/08/14)

QUANTUM FREQUENCY CONVERTER

The single photons emitted by both quantum dots are independently fed into two identical, but distinct frequency converters. At the heart of both conversion setups is an actively temperature stabilized, magnesium oxide doped, periodically poled lithium niobate (MgO:PPLN) waveguide chip (*NTT electronics*) with allover 18 waveguides. All waveguides have a rectangular cross section of (11x10) µm^2 and a length of 40 mm. In order to minimize coupling losses, the end facets have an anti-reflective (AR) coating transparent for all participating light-fields. The chip comes with 9 different poling-periods ranging from 24.300 µm to 24.500 µm. The periodic poling provides quasi-phase matching for a difference frequency generation (DFG) process transducing the input photons at $\lambda_{\mathrm{QD1}} = 904.442$ nm and $\lambda_{\mathrm{QD2}} = 904.420$ nm to the telecom C-band at $\lambda_{\mathrm{tel}} = 1557.28$ nm. To achieve high conversion efficiencies, the process is stimulated by the presence of a pump light field, whose wavelength λ_{p} fulfills the energy conservation relation of the DFG process $1/\lambda_{\mathrm{p}} = 1/\lambda_{\mathrm{QD}} - 1/\lambda_{\mathrm{tel}}$. This corresponds to $\lambda_{\mathrm{p}} = 2157.46$ nm and 2157.32 nm for QD1 and QD2, respectively. Each conversion setup is equipped with a single-frequency tunable Cr^{2+}:ZnS/Se Laser (*IPG Photonics*) as pump light source. For power and polarization control, the pump beam passes a half-wave plate and a Glan-Taylor Calcite Polarizer. Both input light fields are spatially overlapped on a dichroic mirror and coupled to the waveguide via an aspherical zinc selenide lens with a focal length of 11 mm. Subsequent to the conversion, the telecom photons are separated from the pump light by dichroic mirrors, coupled into a single-mode fiber and forwarded to analysis or further experiments. Due to anti-Stokes Raman scattering [1] and a number of non-phase-matched nonlinear conversion processes acting on the pump light, a significant amount of background photons around the target wavelength are created whilst conversion. To minimize this unwanted contribution, the telecom photons are passed from a 1550-20 nm bandpass filter as well as a system of a fiber circulator and a fiber Bragg grating, which acts as an additional 121 GHz broad bandpass filter. At pump light powers of 488 mW and 338 mW the converters reach their maximal external conversion efficiencies of 34.7 % and 31.4 % for QD1 and QD2 as shown in Figure 1. The external conversion efficiency

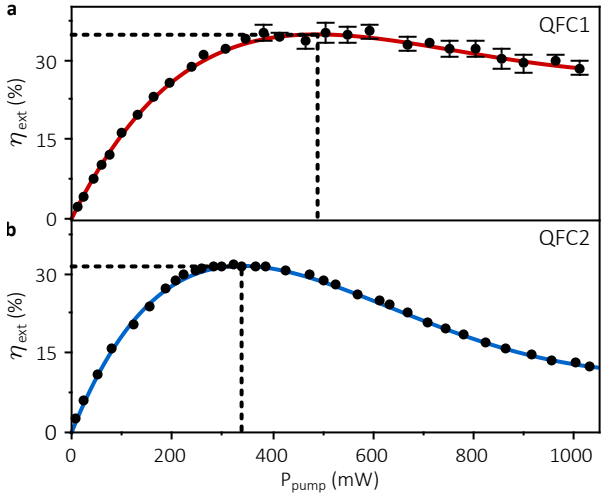

FIG. 1. Converter efficiency versus pump laser power for the two independent QFCs of QD1 (a) and QD2 (b). The maximum conversion efficiency η_{max} is marked as dotted line being $\eta_{\mathrm{max}}^{\mathrm{QFC1}} = 34.7\,\%$ and $\eta_{\mathrm{max}}^{\mathrm{QFC2}} = 31.4\,\%$.

was measured between converter input and output of the FBG filter stage and is defined as the fraction of usable converted photons over input photons.

PUMP LASER STABILITY

The tuning precision of the telecom photons is of utmost importance. As described before, the wavelength of the output photons is set by the pump laser wavelength, which can be controlled in a range from 2000 nm to 2400 nm with MHz precision. In order to monitor the output frequencies f_1 and f_2 of the pump lasers for conversion of QD1 and QD2, the residual pump light is frequency doubled by means of a temperature stabilized MgO:PPLN bulk crystal subsequent to the conversion and then forwarded to a fiber based MEMS-switch. Here, both pump beams are combined before entering a wavemeter (*High Finesse, WS6-200*). To validate the desired detuning $\delta\nu_{\mathrm{pump}} = f_1 - f_2$, both output frequencies f_1 and f_2 were continuously monitored throughout all experiments. Additionally, the stability of the pump laser detuning $\delta\nu_{\mathrm{pump}}$ was tested in a long-time measurement (approx. 11 h) of f_1 and f_2. Both frequencies fluctuate with a rms level of $3\sigma = 78$ MHz. However, both lasers are operated at the same lab and therefore exposed to

the same environmental conditions. Accordingly, their output wavelengths do not drift independently. As a result, the relative pump laser detuning $\delta\nu_{\mathrm{pump}}$ fluctuates with a rms level as low as $3\sigma = 20\,\mathrm{MHz}$ around its mean value $\langle\delta\nu_{\mathrm{pump}}\rangle$, which equals to the resolution limit of the used wavemeter (see Fig. 1d, main text). As this is around 2 orders of magnitude below the FWHM of the recorded tuning curve, it can be assumed that the conversion does not add any relevant frequency jitter to the telecom photons.

THEORY

In the present work, two-photon coalescence of single-photons emitted by two remote QDs is investigated. The photons emerge from a recombination process of charged excitons subsequent to a short, pulsed excitation step. In good approximation the relaxation dynamics can be described by the spontaneous emission of single photons from an ideal two-level system. Accordingly, the photon wave-functions $\zeta_{1,2}(t)$ can be written as

$$\zeta_{1,2}(t) = \frac{1}{\sqrt{\tau_{1,2}}} \cdot \mathrm{H}(t) \cdot e^{-\frac{t}{2\tau_{1,2}} - i2\pi\nu_{1,2}t}, \tag{1}$$

where $\tau_{1,2}$ denotes the radiative lifetime of the charged exciton state, $\nu_{1,2}$ its instantaneous emission frequency and $\mathrm{H}(t)$ the Heaviside-function. Moreover, the QDs are subject to spectral diffusion appearing as a jitter of their emission frequencies. Typically, this leads to an inhomogeneous broadening of the spectral line shape following a normal distribution $p_{1,2}(\nu_{1,2})$ around the mean frequency $\nu_{\mathrm{c},1,2}$ of the QD with standard deviation $\sigma_{1,2}$ according to

$$p_{1,2}(\nu_{1,2}) = \frac{1}{\sigma_{1,2}\sqrt{2\pi}} \cdot \exp\left[-\frac{1}{2}\left(\frac{\nu_{1,2} - \nu_{\mathrm{c},1,2}}{\sigma_{1,2}}\right)^2\right]. \tag{2}$$

The theoretical description of HOM experiments for the given situation is studied in Ref. [2]. The results therein are used in the present work to assess the remote TPI measurements as shown in Figure 1e, main article, as well as to predict the tuning curve in Figure 2, main article. For a better understanding of the underlying equations, the key steps of the derivation shown in Ref. [2] are briefly summarized in the following.

The derivation starts from a well-established formalism describing the HOM experimental situation with the photon fields $\zeta_{1,2}(t)$ at the two inputs of a BS, respectively [3]. Therein, the probability $P(t_0, \tau)$ with which both input photons leave the BS through distinct output ports and become detected at times t_0 and $t_0 + \tau$ is given by

$$P(t_0, \tau) = \frac{1}{4}\left|\zeta_1(t_0+\tau)\,\zeta_2(t_0) - \zeta_2(t_0+\tau)\,\zeta_1(t_0)\right|^2. \tag{3}$$

Using the wave-functions (1), the second-order cross-correlation $g^{(2)}(\tau)$ can be evaluated to

$$\begin{aligned} g^{(2)}(\tau) &= \int_{-\infty}^{+\infty} P(t_0, \tau)\,\mathrm{d}t_0 \\ &= \frac{1}{4(\tau_1+\tau_2)} \times \\ &\left(e^{-\frac{|\tau|}{\tau_1}} + e^{-\frac{|\tau|}{\tau_2}} - 2\cdot e^{-\frac{|\tau|}{2T}}\cos 2\pi\Delta\nu\tau\right), \end{aligned} \tag{4}$$

where the instantaneous emission frequency displacement is described by $\Delta\nu = \nu_1 - \nu_2$ and $1/T = 1/\tau_1 + 1/\tau_2$. During a long-time measurement $\Delta\nu$ does not stay constant, but is subject to jitter due to the independent spectral diffusion processes of both QDs. For a measurement, which takes much longer than the time both emitters need to explore their frequency ranges (2), the probability ρ to find a given splitting $\Delta\nu$ is simply given by the cross-correlation of p_1 and p_2

$$\begin{aligned} \rho(\Delta\nu) &= \int_{-\infty}^{+\infty} p_1(\nu)\,p_2(\nu+\Delta\nu)\,\mathrm{d}\nu \\ &= \frac{1}{\Sigma\sqrt{2\pi}} \cdot \exp\left[-\frac{1}{2}\left(\frac{\Delta\nu + \delta\nu}{\Sigma}\right)^2\right]. \end{aligned} \tag{5}$$

Here, $\delta\nu = \nu_{c,1} - \nu_{c,2}$ is the relative displacement of both mean emission frequencies and $\Sigma^2 = \sigma_1^2 + \sigma_2^2$ defines the width of ρ. Accordingly, the measured cross-correlation $\mathcal{G}^{(2)}(\tau)$ in the long-time limit is obtained by a weighted average of equation (4) using $\rho(\Delta\nu)$ leading to

$$\begin{aligned} \mathcal{G}^{(2)}(\tau) &= \int_{-\infty}^{+\infty} \rho(\Delta\nu)\,g^{(2)}(\tau, \Delta\nu)\,\mathrm{d}\Delta\nu \\ &= \frac{1}{4(\tau_1+\tau_2)} \times \\ &\left(e^{-\frac{|\tau|}{\tau_1}} + e^{-\frac{|\tau|}{\tau_2}} - 2\cdot e^{-\frac{|\tau|}{2T}} e^{-2\pi^2\Sigma^2\tau^2}\cos 2\pi\delta\nu\tau\right). \end{aligned} \tag{6}$$

This is the final result used to describe the central peaks around $\tau = 0$ for all remote TPI correlation measurements shown in the present work.

The visibility of HOM-interference is defined by $V = 1 - 2\cdot P$, where P is the overall probability of both photons going separate ways after meeting at the BS. Accordingly, P can be calculated by integrating equation (6) with respect to the timelag τ. Using the variable $z = (2\pi\delta\nu + i/2T) / \left(2\pi\sqrt{2}\Sigma\right)$, the visibility evaluates to

$$V = \frac{\mathrm{Re}\left[w(z)\right]}{\sqrt{2\pi}\Sigma(\tau_1+\tau_2)}, \tag{7}$$

where the Faddeeva function $w(z)$ [4, Chap. 7] is used to express the result. Equation (7) is the definition of a Voigt line shape as a function of the detuning $\delta\nu$, whose width is given by the homogeneous contributions $\tau_{1,2}$ and

inhomogeneous contributions $\sigma_{1,2}$. Thus, the visibility of a remote HOM experiment is determined by the joint spectral properties of both emitters. Equation (7) is used in the present work to predict the experimentally achieved visibilities as function of the pump laser detuning for the remote HOM case (see Figure 2, main text). Equation (7) can be also written in terms of the error function shown in Equation (4) of the main article.

DATA ANALYZATION

All correlation histograms are based on time tagging of the raw coincidence events with a *HydraHarp400* with a binning resolution of 1 ps. The obtained data is averaged via convolution with the detector response, being $\Delta\tau_{\mathrm{SNSPD}} \simeq 100\,\mathrm{ps}$ for all data beside the data in Figure 2b-d of the main article where $\Delta\tau_{\mathrm{SNSPD}} \simeq 40\,\mathrm{ps}$. Furthermore, all data is background corrected. Each correlation histogram is accompanied with a model which is based on Eq. (6). The model is predetermined by the transition lifetimes $\tau_{1,2}$, inhomogeneous broadening, reflected via $\Sigma^2 = \sigma_1^2 + \sigma_2^2$, where $\sigma_i = \mathrm{FWHM}_i/(2\sqrt{2\log 2})$, and the spectral detuning $\delta\nu_{\mathrm{QDs}}$ between the two QDs. In order to have an independent access to the actually measured TPI visibility, each correlation measurement has a correlation window being larger than 1 µs. This allows to take into account the Poissonian level being the temporally uncorrelated time regime. Comparison between center peak area and the Poissonian level then delivers the TPI visibility (further information on how to access V_{TPI} can be found in Ref. [5]). The error of the measured TPI visibilities is determined via error-propagation, taking the standard errors of center peak and Poissonian level (calculated via $\sqrt{N}$, where N is the number of coincidence events) as well as the error of background subtraction into account.

SIMULATION OF TWO-PHOTON OVERLAP AFTER LONG-DISTANCE FIBER-PATH

Starting with the photons temporal shape, Fourier transformation is used to obtain the corresponding spectrum. The propagation is considered via the complex refractive index n_c, where the real part includes dispersion and the imaginary part absorption. The final temporal shape is obtained via inverse Fourier transformation:

$$\chi(t) \overset{\mathcal{FT}}{\longmapsto} \chi_{\mathrm{in}}(\nu) \overset{fiber}{\longmapsto} \chi_{\mathrm{out}}(\nu) \overset{\mathcal{FT}^{-1}}{\longmapsto} \chi_{\mathrm{out}}(t) \qquad (8)$$

where $\chi_{\mathrm{out}}(\nu) = \chi_{\mathrm{in}}(\nu) \cdot e^{in_c kL}$. Within the simulations the refractive index of the fiber is considered via an approximation given in the datasheet of the used *SMF-28 Ultra Optical Fiber* by *Corning*. The dispersion value D is given as

$$D(\lambda) \approx \frac{S_0}{4}\left(\lambda - \frac{\lambda_0^4}{\lambda^3}\right) \qquad (9)$$

where S_0 is the zero dispersion slope, λ_0 the zero dispersion wavelength and λ the operating wavelength. The relation $\mathrm{d}n/\mathrm{d}\lambda = c \cdot D$ yields the refractive index. Additionally, the absorption was assumed to be approximately constant and was also given in the data sheet. The temporal shapes of the photons after propagation through a fiber of a certain distance are used to calculate the TPI spectrum. And therefore it is possible to extract the respective visibility.
For the investigated QD-pair, inhomogeneous broadening was additionally considered. Therefore, the spectra of QD1 and QD2 were numerically expressed as Gaussian frequency distributions including the measured FWHM. Then, random photon pairs from the two independent distributions were chosen. Using the same method as above, the photon of QD2 was sent through the virtual fiber. Each data point of this curve in Fig. 4 is the mean of 500 photon pairs. The absolute error of all three numeric curves is estimated to be 1 % in TPI visibility. Further information on the simulation method can be found in Reference [6].

SPECTRAL DIFFUSION

As discussed in course of our theoretical model, the key properties, which drive the indistinguishability of photons from two remote QDs are the integrated emission spectra, including all broadening mechanisms, as well as the lifetime of the addressed state. Spectral diffusion can be quantified by fitting a Voigt profile to the spectral distribution (see main text Fig. 1b) while fixing homogeneous broadening to $\Delta\nu_{\mathrm{homog}} = 0.27\,\mathrm{GHz}$, an estimation based on decay times $\tau_{\mathrm{dec,QD1}} = (580 \pm 10)\,\mathrm{ps}$ and $\tau_{\mathrm{dec,QD2}} = (600 \pm 10)\,\mathrm{ps}$ of the two QDs. Actual inhomogeneous broadening can then be extracted, here resulting in $\mathrm{FWHM}_{\mathrm{QD1}} = (2.0 \pm 0.1)\,\mathrm{GHz}$ and $\mathrm{FWHM}_{\mathrm{QD2}} = (1.3 \pm 0.1)\,\mathrm{GHz}$. Consequently, time-correlated single-photon counting (TCSPC) and hPL are sufficient to predict the indistinguishability of photons from remote QDs. In contrast, when performing such an experiment with an individual QD it is much more complex to predict the TPI visibility as the spectral diffusion time constant drive the frequency correlation between interfering photons. Figure 2a shows an unbalanced Mach-Zehnder Interferometer (MZI) with time-delay τ_{MZI} being either 4 ns or 10 µs (realized by inserting 2 km of additional fiber path length). Figure 2b,c shows TPI measurements with photons consecutively emitted from QD2, for the two above mentioned time delays. As the time difference is increased from 4 ns to 10 µs, the photon indistinguishability is decreased from $V_{\mathrm{QD2}}^{4\,\mathrm{ns}} = (61 \pm 3)\,\%$ (this com-

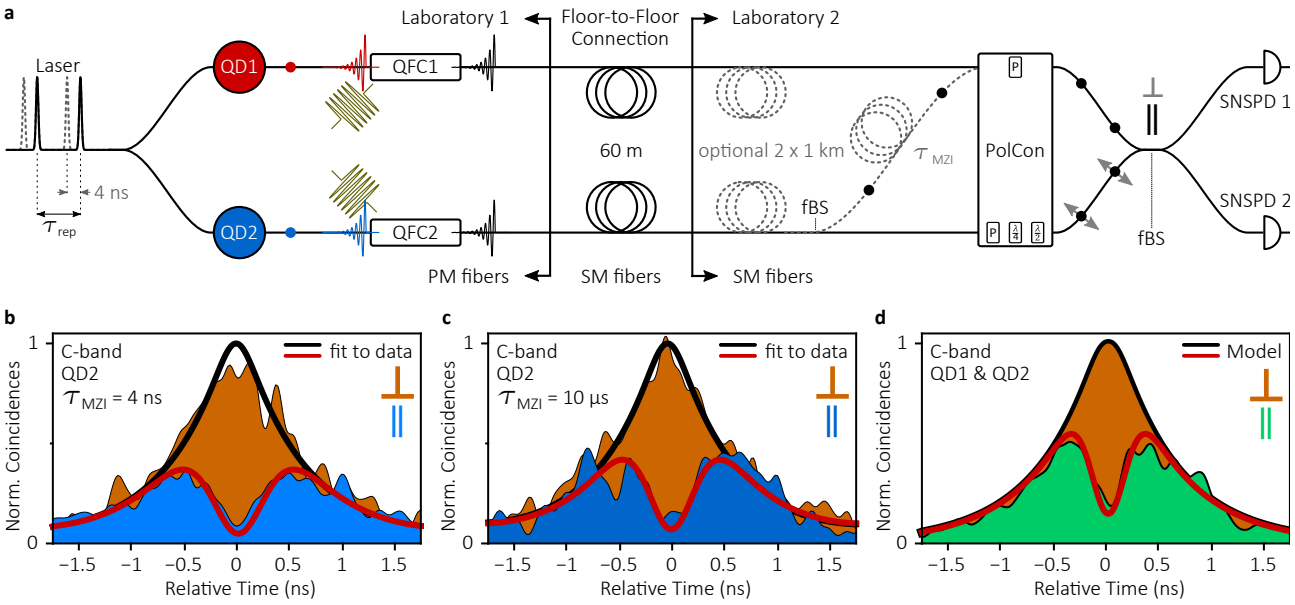

FIG. 2. (a) Sketch of experimental setup utilized for TPI measurements of consecutively emitted photons (dotted line configuration for QD2) as well as TPI with remote QDs situated in distinct cryostats (solid line configuration). In both configurations, the emission is transferred to the telecom C-band via two distinct frequency converters named QFC1 and QFC2. A polarization control (PolCon) is used to fix the polarization in both interferometer arms and to realize distinguishable ($\perp$) and indistinguishable ($\parallel$) photon overlap on a fiber-based beamsplitter (fBS). Detected events are time-tagged for the following correlation analysis. (b,c) Center correlation peak of TPI measurements with consecutively emitted photons of QD2 for $\tau_{\mathrm{MZI}} = 4\,\mathrm{ns}$ and $\tau_{\mathrm{MZI}} = 10\,\mu\mathrm{s}$ delay of the MZI normalized to the case with distinguishable photons. (d) Remote TPI measurement with QD1 and QD2 on spectral resonance with parallel and orthogonal polarization setting.

pares well with the corresponding NIR experiment giving $V_{\mathrm{QDB}}^{4\,\mathrm{ns}} = (60 \pm 3)\,\%$ [5]) to $V_{\mathrm{QD2}}^{10\,\mu\mathrm{s}} = (48 \pm 5)\,\%$. Equation (7) is further giving the TPI visibility in the fully uncorrelated time regime, i.e., $\tau_{\mathrm{MZI}} \gg 10\,\mu\mathrm{s}$. Using the emission properties of QD2 it returns $V_{\mathrm{QD2,\,sim}}^{\mathrm{remote}} = (33 \pm 1)\,\%$. Consequently, the spectral diffusion constant of QD2 is beyond 10 µs. This is further supported when comparing with Figure 2d. Being not far apart in inhomogeneous broadening, the remote TPI experiment with QD1 and QD2 leads to $V_{\mathrm{exp}}^{\mathrm{remote}} = (29 \pm 3)\,\%$.

ENTANGLEMENT DISTRIBUTION

We estimate an entanglement distribution rate based on the quantum repeater protocol presented by Sangouard et al. [7]. In this case the quantum dots are solely used as single photon emitter in combination with a quantum memory. For the estimation, parameters like TPI visibility, entanglement fidelity, etc. are set to be ideal. Then, each attempt to create an entangled state succeeds with a probability given by

$$P_0 = 2 p_1 \beta^2 \eta\, \eta_{\mathrm{QFC}} \tag{10}$$

with probability p_1 that a single photon is emitted and β^2 the beam splitter transmissivity giving the probability that the photon travels towards the central station. The efficiency η summarizes all losses due to non-ideal collection, coupling and detection efficiencies as well as transmission losses in the optical path. The conversion efficiency is denoted η_{QFC}. Multiplying P_0 with the repetition rate ν_{rep}, we obtain the desired entanglement generation rate ν_{ent}

$$\nu_{\mathrm{ent}} = P_0 \nu_{\mathrm{rep}} = 2 p_1 \beta^2 \eta\, \eta_{\mathrm{QFC}} \nu_{\mathrm{rep}} = 2 \beta^2 \nu_{\mathrm{det}}. \tag{11}$$

Here, we used the fact that the count rate $\nu_{\mathrm{det}} = 7\,\mathrm{kHz}$ obtained in our present experiment is determined by repetition rate, photon emission probability and all efficiencies according to $\nu_{\mathrm{det}} = p_1 \eta \eta_{\mathrm{QFC}}\, \nu_{\mathrm{rep}}$. To minimize the probability that both photons are forwarded to the central station, β^2 is typically chosen small. Assuming $\beta^2 = 0.1$ we obtain an entanglement generation rate of $\nu_{\mathrm{ent}} = 1.4\,\mathrm{kHz}$. We note that this rate, however, should be seen as upper bound as it yields the rate of successful detection events only. To use the entangled states of the memory one has to wait for the arrival of the classical signal heralding the successful detection event (which decreases the potential repetition rate, depending on the communication distance) and one has to employ the entangled memory states e.g. for creation of a secret key bit. The duration and fidelity of this operation, however, depends strongly on the chosen protocol such that an elaborate discussion would by far exceed the scope of our manuscript.

* These authors contributed equally
† s.portalupi@ihfg.uni-stuttgart.de
‡ p.michler@ihfg.uni-stuttgart.de; www.ihfg.physik.uni-stuttgart.de

[1] Zaske, S., Lenhard, A. & Becher, C. Efficient frequency downconversion at the single photon level from the red spectral range to the telecommunications C-band. *Optics Express* **19**, 12825 (2011).

[2] Kambs, B. & Becher, C. Limitations on the indistinguishability of photons from remote solid state sources (2018). arXiv: 1806.08213.

[3] Legero, T., Wilk, T., Kuhn, A. & Rempe, G. Time-resolved two-photon quantum interference. *Appl. Phys. B* **77**, 797–802 (2003).

[4] Abramowitz, M. & Stegun, I. A. *Handbook of mathematical functions: with formulas, graphs, and mathematical tables*. Dover books on advanced mathematics (Dover Publications, New York, 1964).

[5] Weber, J. H. *et al.* Overcoming correlation fluctuations in two-photon interference experiments with differently bright and independently blinking remote quantum emitters. *Phys. Rev. B* **97**, 195414 (2018).

[6] Vural, H. *et al.* Two-photon interference in an atom-quantum dot hybrid system. *Optica* **5**, 367 (2018).

[7] Sangouard, N., Simon, C., de Riedmatten, H. & Gisin, N. Quantum repeaters based on atomic ensembles and linear optics. *Reviews of Modern Physics* **83**, 33–80 (2011).